Chapter 5
Attenuation of High-Frequency Seismic Waves

We will now discuss the attenuation with propagation distance of seismic wave amplitude in the lithosphere for frequencies mostly higher than 1 Hz. First we review the frequency dependence of observed amplitude attenuation in the earth's lithosphere. We discuss various proposed mechanisms of intrinsic attenuation and describe their frequency characteristics. We have already discussed the scattering of seismic waves caused by random heterogeneities as a mechanism to explain the excitation of S-coda waves. The amplitude decay with travel distance will now be derived as a natural consequence of the energy conservation; scattering attenuates the direct wave amplitude and excites coda waves. Taking scalar waves as an example, we present an approach for calculating the amount of scattering attenuation in a manner consistent with conventional seismological attenuation measurements. Then, extending the method to elastic waves, we calculate the scattering attenuation of P- and S-waves in randomly inhomogeneous elastic media. The randomness of the lithosphere will then be quantitatively estimated from S-wave attenuation and S-coda excitation measurements. We will briefly introduce scattering attenuation due to distributed cracks and cavities.

5.1 Measurements of Attenuation in the Lithosphere

Seismic wave amplitude generally decreases with increasing travel distance through the earth. Except where wave interference occurs, the observed amplitude usually decreases exponentially with travel distance, and the decay rates are proportional to Q_P^{-1} and Q_S^{-1} which characterize the spatial attenuation for P- and S-waves, respectively. For spherically outgoing body waves in a uniform velocity structure in a 3-D space, there is an additional geometrical spreading factor r^{-1}, so the spectral amplitudes of P- and S-waves, u^P and u^S at frequency f, go roughly as

$$u^P(r; f) \propto \frac{e^{-\pi r f Q_P^{-1}/\alpha_0}}{r} \quad \text{and} \quad u^S(r; f) \propto \frac{e^{-\pi r f Q_S^{-1}/\beta_0}}{r}. \tag{5.1}$$

A popular method of making attenuation measurements is the spectral decay method, which uses measurements of spectral amplitudes vs. frequency for at least two propagation distances. If we know $u^P (r_1; f)$ and $u^P (r_2; f)$,

$$\ln \frac{r_2 u^P (r_2; f)}{r_1 u^P (r_1; f)} = -\pi(r_2 - r_1) f Q_P^{-1}/\alpha_0 + \text{Const.} \tag{5.2}$$

If Q_P^{-1} is assumed to be frequency independent, its value can be determined from the slope of the left-hand side of (5.2) vs. f from data at a single station. More accurate measurements are made by using two stations and two sources. Other measurements have been based on observations of the change in direct-wave amplitude with distance using the coda-normalization method with data from a single station as mentioned in Sect. 3.3.3. More recent Q_S^{-1} measurements have been based on the multiple lapse-time window analysis of whole S-wave seismograms, which will be discussed in Sect. 8.1.4.

We summarize recent measurements of Q_S^{-1}, Q_P^{-1} and the ratio Q_P^{-1}/Q_S^{-1} in the lithosphere in Figs. 5.1, 5.2 and 5.3, respectively. As shown in Fig. 5.1, measurements in North America show that Q_S^{-1} takes large values in tectonically active areas as Basin and Range Province and California compared with stable areas as central and northeastern U.S.A. and southeastern Canada (see lines 2.1–2.3, 30.1–30.3) (e.g. Benz et al. 1997; Mitchell 1995). Though the scatter is as large as factor 2 or 3, attenuation Q_S^{-1} roughly takes the maximum value of the order of 0.01 around 1 Hz. Attenuation Q_S^{-1} decreases with increasing frequency according to a power of frequency as $Q_S^{-1} \propto f^{-n}$, where the exponent n rages from 0.5 to 1. Attenuation Q_S^{-1} takes the value of the order of 0.001 at 20 Hz. The behavior of attenuation Q_S^{-1} bellow 1 Hz is not clear; however, Aki (1980a,b) conjectured that Q_S^{-1} decreases with decreasing frequency for frequencies lower than 1 Hz. Later Kinoshita (1994) observed Q_S^{-1} having a peak around 1 Hz from measurements in southern Kanto, Japan (line 16). As shown in Fig. 5.2, the number of measurements of Q_P^{-1} is not large enough as that of Q_S^{-1}; however, we find that Q_P^{-1} decreases with frequency from 1 Hz to 20 Hz. From surface wave measurements, ratio Q_P^{-1}/Q_S^{-1} in the lithosphere has been taken to be constant at $0.4 - 0.47$ by many investigators for frequencies less than 0.05 Hz . For frequencies higher than 1 Hz, however, most of recent measurements have clearly shown that the ratio Q_P^{-1}/Q_S^{-1} ranges between 1 and 2, and sometimes up to 3.

5.2   Intrinsic Attenuation Mechanisms

The mechanism of seismic wave attenuation has been a topic of interest among seismologists and rock physicists for many years and numerous physical mechanisms to explain the cause of seismic wave attenuation have been proposed. Seismic attenuation is usually considered to be caused by two mechanisms, scattering and
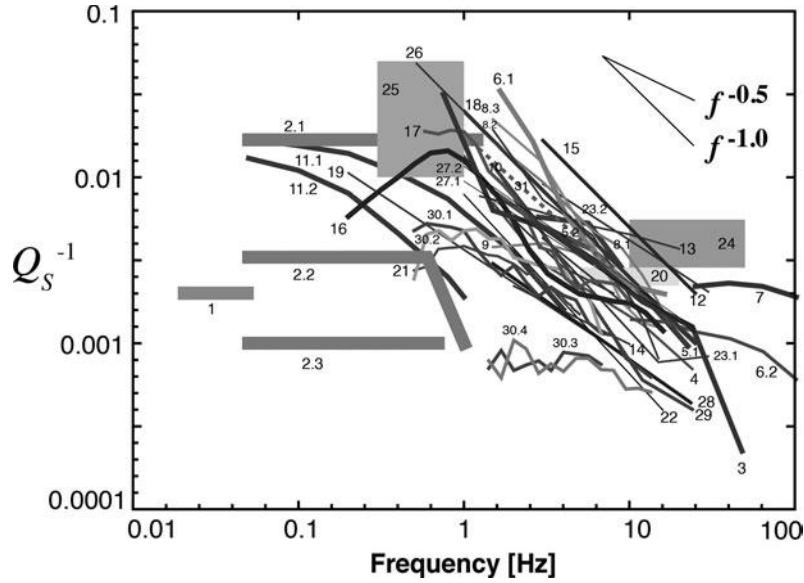
Fig. 5.1 Reported values of Q_S^{-1} for the lithosphere: 1 Crust of the SL8 global model (Anderson and Hart 1978), 2.1 Tectonic upper crust, 2.2 Stable upper crust, 2.3 Lower crust (Mitchell 1995), 3 Hindu–Kush (Roecker et al. 1982), 4 Kanto, Japan (Aki 1980a), 5.1 Eastern Kanto, Japan (Sato and Matsumura 1980), 5.2 Kanto, Japan (Yoshimoto et al. 1993), 6.1 Surface data, 6.2 Borehole data in S. California (Adams and Abercrombie 1998), 7 Shallow crust at western Nagano, Japan (Yoshimoto et al. 1998), 8.1 Central California, 8.2 Hawaii, 8.3 Long Valley in California, U.S.A. (Mayeda et al. 1992), 9 Kanto-Tokai, Japan (Fehler et al. 1992), 10 Kyushu, Japan (Hoshiba 1993), 11.1 Basin and Range Province, 11.2 U. S. Shield (Taylor et al. 1986), 12 Sg and Lg, Utah, U.S.A. (Brockman and Bollinger 1992), 13 Depth 5–25 km, southern Kurils (Fedotov and Boldyrev 1969), 14 Lg, France (Campillo and Plantet 1991), 15 Imperial fault, California (Singh et al. 1982), 16 Depth < 50 km, southern Kanto, Japan (Kinoshita 1994; Kinoshita and Ohike 2002), 17 E. Honshu, Japan (Kato et al. 1998), 18 Montenegro, Yugoslavia (Rovelli 1984), 19 Mexico (Ordaz and Singh 1992), 20 Depth < 40 km, northern Caribbean (Frankel 1982), 21 Colombia (Ojeda and Ottemöller 2002), 22 Southern Norway (Kvamme and Havskov 1989), 23.1 New York State, U.S.A., 23.2 Southern California (Frankel et al. 1990), 24 Depth < 10 km, Arette, Pyrénées (Modiano and Hatzfeld 1982), 25 San Andreas Fault, California (Kurita 1975), 26 Southern Italy (Rovelli 1983), 27.1, SV, 27.2, SH, Marche, Italy (Castro et al. 1999), 28 SE Korea (Chung and Sato 2001), 29 Bhuj, India (Padhy 2009), 30.1 Basin Range Province, 30.2 South and South Central California, 30.3 Central United States, 30.4 N. E. United States and S.E. Canada (Benz et al. 1997), 31 Kirishima volcano, Kyushu, Japan (Izutani 2000)

intrinsic mechanisms, so that total attenuation is the sum of the two types:

$$Q_P^{-1} = {}^{Sc}Q_P^{-1} + {}^{I}Q_P^{-1} \quad \text{and} \quad Q_S^{-1} = {}^{Sc}Q_S^{-1} + {}^{I}Q_S^{-1}. \tag{5.3}$$

As we have seen, scattering redistributes wave energy within the medium but does not remove energy from the overall wavefield. Conversely, intrinsic attenuation refers to various mechanisms that convert vibration energy into heat through
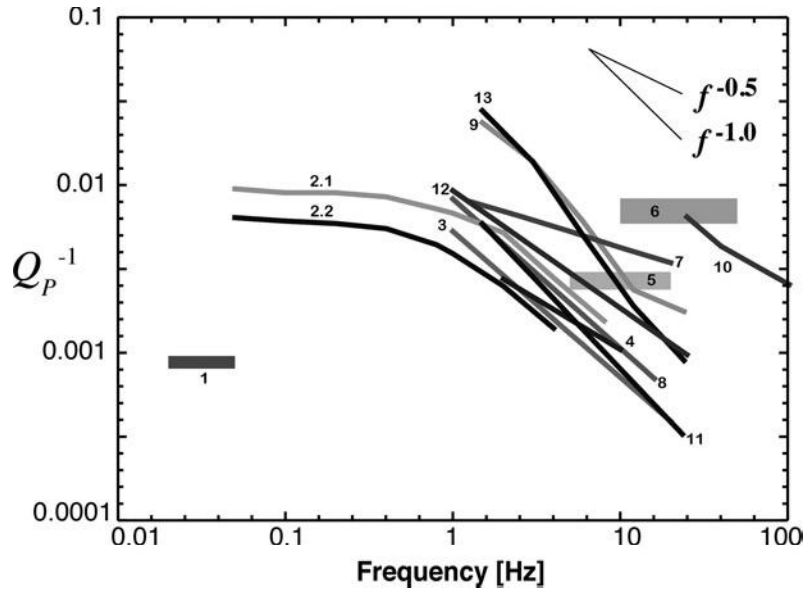
Fig. 5.2 Reported values of Q_P^{-1} for the lithosphere: 1 Depth < 45 km of the SL8 global model (Anderson and Hart 1978), 2.1 Basin and Range Province, 2.2 U. S. Shield (Taylor et al. 1986), 3 Pn, eastern Canada (Zhu et al. 1991), 4 Pg, France (Campillo and Plantet 1991), 5 Depth < 40 km, northern Caribbean (Frankel 1982), 6 Depth < 10 km, Arette, Pyrénées (Modiano and Hatzfeld 1982), 7 Depth $5-25$ km, southern Kurils (Fedotov and Boldyrev 1969), 8 Southern Norway (Kvamme and Havskov 1989), 9 Kanto, Japan (Yoshimoto et al. 1998), 10 Upper crust of western Nagano, Japan (Yoshimoto et al. 1998), 11 Crust, SE Korea (Chung and Sato 2001), 12 Marche, Italy (Castro et al. 1999), 13 Crust, Bhuj, India (Padhy 2009)

friction, viscosity, and thermal relaxation processes. Measurements of attenuation of direct seismic waves give values for total attenuation. There has been considerable speculation about which process, intrinsic or scattering, dominates attenuation and several methods have been proposed to determine the amounts of both scattering and intrinsic attenuation (Fehler et al. 1992; Jacobson 1987).

Models of seismic attenuation were initially developed to explain an apparently observed frequency-independence of Q^{-1} at low frequencies. There are several review papers that discuss proposed mechanisms for intrinsic attenuation that lead to frequency-independent Q_P^{-1} and Q_S^{-1} (e.g. Dziewonski 1979; Jackson and Anderson 1970; Knopoff 1964). Attenuation has been considered an important parameter to measure and characterize sedimentary rocks for petroleum exploration, and this has led to an effort to develop models explaining the observed attenuation in sedimentary rocks (e.g. Mavko et al. 1979; Toksöz and Johnston 1981). Many proposed intrinsic attenuation models are relaxation mechanisms having characteristic relaxation times that depend on the physical dimensions of the elements in the rock. The characteristic time leads to a Q^{-1} that peaks at some frequency and decreases rapidly away from that frequency. By assuming
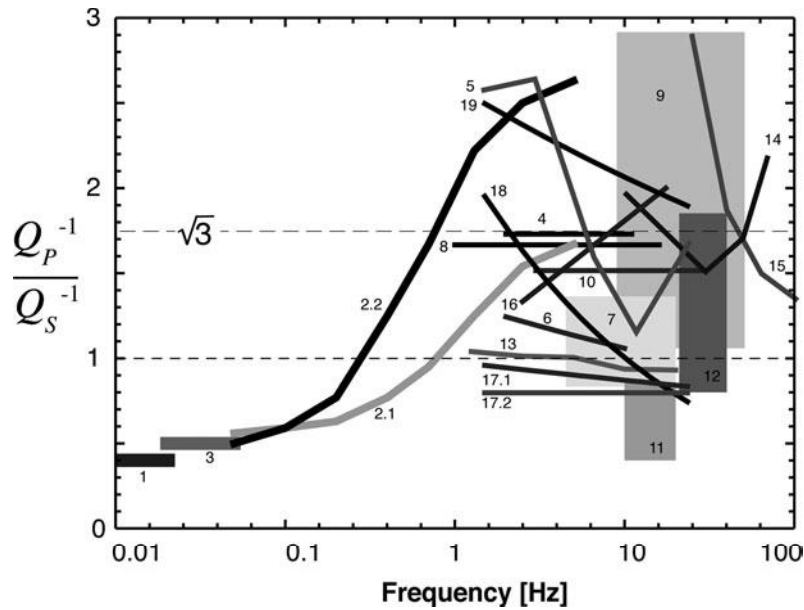
Fig. 5.3 Ratio Q_P^{-1}/Q_S^{-1} for the lithosphere based on measurements of P- and S-wave attenuation: 1 MM8 global model (Anderson et al. 1965), 2.1 Basin and Range Province, 2.2 U. S. Shield (Taylor et al. 1986), 3 Depth <45 km of the SL8 global model (Anderson and Hart 1978), 4 Garm, Central Asia (Rautian et al. 1978), 5 Kanto, Japan (Yoshimoto et al. 1993), 6 Pg and Lg, France (Campillo and Plantet 1991), 7 Depth < 40 km, northern Caribbean (Frankel 1982), 8 Southern Norway (Kvamme and Havskov 1989), 9 Depth < 10 km, Arette, Pyrénées (Modiano and Hatzfeld 1982), 10 Upper crust, Rio Grande Rift, U.S.A. (Carpenter and Sanford 1985), 11 Depth < 7 km, San Andreas Fault (Bakun et al. 1976), 12 Depth < 7 km, Swabian Jura, Germany (Hoang-Trong 1983), 13 Southern Kurils (Fedotov and Boldyrev 1969), 14 Anza, California (Hough et al. 1988), 15 Upper crust of western Nagano, Japan (Yoshimoto et al. 1998), 16 Western Pacific (Butler et al. 1987), 17.1 P/SV, 17.2 P/SH, Marche, Italy (Castro et al. 1999), 18 Crust, SE Korea (Chung and Sato 2001), 19 Crust, Bhuj, India (Padhy 2009)

that rocks are composed of elements with a range of dimensions, the attenuation caused by the mechanism can be made frequency-independent over some frequency range. For seismic waves to remain causal, there must be frequency dependence in wave velocity and intrinsic attenuation $^I Q^{-1}$ (Aki and Richards 1980; Azimi et al. 1968, p.173). The relationship between frequency-dependent attenuation and velocity dispersion was discussed by Liu et al. (1976).

Although we will not describe all proposed mechanisms of intrinsic attenuation, we will briefly examine some and give their predicted relation between physical dimensions and characteristic frequencies. Our discussion follows closely that of Aki (1980a). Many of the papers we will refer to have been reprinted in Toksöz and Johnston (1981). Models whose characteristic frequencies are well removed from the frequency band of observed regional seismic phases cannot be considered as the dominant attenuation mechanisms in that band. Any viable model must be consistent

with the observed and partially conjectured frequency-dependence of Q_S^{-1} having a peak on the order of 0.01 around 0.5 Hz.

Many proposed mechanisms of intrinsic attenuation are based on the observation that crustal rocks have microscopic cracks and pores which may contain fluids. These features have dimensions much smaller than the wavelengths of regional seismic phases. As discussed in Chap. 2, these cracks can have a profound influence on the propagation velocity of P- and S-waves through rocks (see Fig. 2.1). Crack aspect ratio d, which is the ratio of width to length of a crack, is one of the dominant parameters controlling the frequency-dependence of many attenuation models. Hadley (1976) used a scanning electron microscope to measure crack lengths and aspect ratios of virgin and prestressed samples of Westerly granite. She found crack lengths up to 150 microns and aspect ratios of 10^{-4} to 10^{-1}. Walsh (1966) proposed frictional sliding on dry surfaces of thin cracks as an intrinsic attenuation mechanism. The frictional model predicts that $^I Q^{-1}$ is frequency-independent over the frequency range of regional seismic phases. Walsh (1969) proposed viscous dissipation of energy due to liquid movement through cracks as another attenuation mechanism. This model predicts a peak in attenuation at frequency $d\mu/2\pi\eta$, where μ is the rigidity of the surrounding rock and η is the viscosity of the fluid. If water fills the pores, the viscosity $\eta \approx 10^{-2}$ poise at $20\,^\circ$C decreases with increasing temperature and increases with increasing pressure (Keenan et al. 1969). By using $\mu \approx 10^{12}\,\text{g/cm}^2$ for rocks and the range of aspect ratios for rocks found by Hadley (1976), this model predicts an attenuation peak at $10^9 \sim 10^{12}$ Hz. To get a peak frequency at 0.5 Hz would require aspect ratios of $d \approx 3 \times 10^{-14}$, which is inconsistent with Hadley's (1976) measurements.

Nur (1971) proposed viscous dissipation in a zone of partially molten rock to explain the low velocity and high attenuation zone at the base of the lithosphere. The addition of water reduces the melting temperature of rocks; however, the melting temperature at 15 kb is $600\,^\circ$C for granite, and it is $800\,^\circ$C for peridotite (Boettcher 1977). At the Moho depths beneath Kanto, Japan, that is located in the fore-arc side of the VF, the temperature is estimated to be $200 - 300^\circ$C (Uyeda and Horai 1964), which is unlikely to melt rocks. Biot (1956a,b) analyzed wave propagation in isotropic porous solids where the coupling of motion between the fluid and the solid matrix was considered. He arrived at expressions for attenuation due to the flow of fluids within non-connecting pores initiated by elastic waves. White [1965, p.131] discussed Biot's models and concluded that the attenuation predicted by this model was extremely small for frequencies less than 100 Hz. He showed that the model included the loss of elastic energy only through viscous drag on the fluid at the crack walls and that this loss was too small to be consistent with seismic measurements. Mavko and Nur (1979) examined the effect of partial saturation of cracks on attenuation. In their model, fluid movement within cracks is enhanced by the presence of gas bubbles, and predicted attenuation is larger than that in Biot's (1956a; 1956b) models. The partial saturation model has a peak attenuation at frequency $\sqrt{K_f/\rho_f}/2\pi a_f$, where K_f is the fluid bulk modulus, ρ_f the fluid density and a_f the half-length of the fluid drop in the crack: $^I Q^{-1}$

is proportional to $\omega^{3/2}$ for lower frequencies and to $\omega^{-3/2}$ at higher frequencies. For water, $K_f \approx 10^{12}$ g/cm·s^2 and $\rho_f \approx 1$ g/cm^3. For attenuation to peak in the regional seismic frequency band, $a_f \approx 10^5$ cm, which is too large. As an alternative to considering just the effects of fluid movement within one crack, O'Connell and Budiansky (1977) proposed a model in which fluid moves between closely spaced adjacent cracks. There is a characteristic frequency corresponding to the transition from saturated isolated to saturated isobaric behaviors: $f \approx Kd^3/2\pi\eta$, where K is the bulk modulus of the rock. This frequency is lower than the peak frequency predicted by Walsh's (1969) viscous dissipation model. When $\eta \approx 10^{-2}$ poise for water and $K \approx 10^{12}$g/cm·s^2, a 0.5 Hz attenuation peak in rock requires aspect ratio $d \approx 10^{-5}$, which is close to a range consistent with Hadley (1976)'s measurements; however, numerical simulation by O'Connell and Budiansky (1977) predicts $Q_P^{-1} < Q_S^{-1}$, which contradicts observations.

After drying an olivine basalt sample in a moderately heated high vacuum, Tittmann (1977) found that Q_P^{-1} decreased from 2×10^{-2} to 0.9×10^{-3} at 56 Hz. Low attenuation for a dry rock is consistent with the very low attenuation values measured on lunar rock samples that contain little water (Tittmann et al. 1976). Gradually adding a small amount of volatile to a dry rock, Tittmann et al. (1980) measured an increase of Q_S^{-1} and a change in electric dipole moment which indicated adsorption of the volatile. They found that the rapid increase of Q_S^{-1} was not due to the classical viscous fluid movement through fractures but due to an interaction between adsorbed water film on the solid surface by thermally activated motions. This is due to relaxation involving liquid molecules. Controlling the amount of water, Spencer (1981) identified individual relaxation peaks in rocks. He found a peak in Q_E^{-1} at frequencies as low as 17 Hz in limestone, where E is Young's modulus. However, the peak frequency is of the order of kHz for other kinds of rocks. He argued that most rocks have a range of relaxation frequencies and that the dominant mechanism of attenuation observed in his measurements is a frequency-dependent softening of the rock due to the bonding of fluid molecules to crack surfaces.

Karato and Spetzler (1990) reviewed experimental studies on intrinsic absorption mechanisms of upper mantle peridotite, and they pointed out the importance of dislocation and/or grain boundary mechanisms (e.g. Anderson and Hart 1978; Lundquist and Cormier 1980). Their frequency dependence is written as $^IQ^{-1} \propto \omega^{-\alpha}\exp(-\alpha E^*/RT)$, where E^* is activation energy. Parameters for olivine-dominated rocks have been constrained by several experiments: α ranges from 0.1 to 0.3 and E^* from 400 to 600 kJ/mol (Karato 2008, Chapter 11). Nakajima and Hasegawa (2003) used this mechanism for the interpretation of frequency-independent Q_P^{-1} measurement of the order of 10^{-3} beneath the VF and the back-arc side of northeastern Honshu, Japan (Tsumura et al. 2000); however, the predicted frequency dependence of this mechanism is too weak.

Spatial temperature differences induced by a passing wave due to adiabatic compression are reduced by thermal diffusion (Savage 1965; Zener 1948). This thermoelastic effect removes vibrational energy from a wavefield. Grain-sized het-

erogeneities in a rock increase the amount of predicted attenuation. Thermoelastic attenuation peaks at frequency D_T/a_g^2, where a_g is the grain size and D_T is the thermal diffusivity. For $D_T \approx 5 \times 10^{-2}$cm^2/s for quartz and a peak frequency of 0.5 Hz, $a_g \approx 0.3$ cm, which is reasonable for rocks. The exchange of heat between adjacent grains plays an important role for Q_P^{-1}. Because of rock hetero-geneity, thermoelasticity causes S-wave attenuation, but it causes more attenuation for compressional waves. Therefore, the model predicts $Q_P^{-1} > Q_S^{-1}$. Savage (1966) investigated thermoelasticity caused by stress concentrations induced by the presence of empty cracks having the shape of elliptic cylinders. This model predicts a peak in attenuation at a frequency given by D_T/a_c^2, where a_c is the half-length of the crack, which yields crack sizes similar to grain sizes predicted by Zener's (1948) model. For ordinary materials containing cracks, the theory predicts $Q_P^{-1} > Q_S^{-1}$, which is consistent with measurements.

Predicted intrinsic attenuation varies with depth, temperature, fracture content, fracture aspect ratios, pressure, and the presence of fluids. Most of the mechanisms discussed above can predict Q_S^{-1} having values in the range of 10^{-3}. Aki (1980a) preferred thermoelasticity as the viable model among various intrinsic attenuation models to explain attenuation having a peak at around 0.5 Hz at lithospheric temperatures.

5.3   Scattering Attenuation in Random Inhomogeneities

A first step in making a model of attenuation is to determine whether it is controlled by some characteristic scale in time or space. In Figs. 5.1–5.3 we took frequency as the abscissa, which allows us to look at characteristic time scales. Figure 3.32b shows Q_S^{-1} and Q_P^{-1} vs. frequency in Kanto, Japan, measured by using an extension of the coda-normalization method (Yoshimoto et al. 1993). Choosing wavenumber as the abscissa allows us to investigate the spatial scale of attenuation. In Fig. 5.4, abscissa is wavenumber, where frequency 0.5 Hz corresponds to S-wave wavenumber of about 0.8 km^{-1}. The results show good coincidence between Q_S^{-1} and Q_P^{-1}. This coincidence implicitly suggests that attenuation is characterized by a spatial scale.

As shown in Fig. 3.31b, attenuation for S-waves Q_S^{-1} is conjectured to have a peak of amplitude about 10^{-2} at about 0.5 Hz and to decrease for both increasing and decreasing frequency away from 0.5 Hz. Figure 5.4 shows that attenuation per travel distance $2\pi f Q_S^{-1}/\beta_0$ is approximately constant for 1 to 20 Hz and has a value on the order of 10^{-2} km^{-1}, which is nearly the same order as the total scattering coefficient g_0 of S-waves as shown in Fig. 1.3. The coincidence leads to the idea that scattering attenuation may be the dominant mechanism for amplitude attenuation of seismic waves in the lithosphere (Aki 1980a, 1981, 1982).

We may expect that scattering attenuates direct wave amplitude and excites coda waves; however, we will show that the conventional derivation of amplitude attenuation using the Born approximation to estimate scattering attenuation leads to

Fig. 5.4 Plots of Q_S^{-1}
(closed circle) and Q_P^{-1}
(triangle) vs. wavenumber
measured in Kanto, Japan.
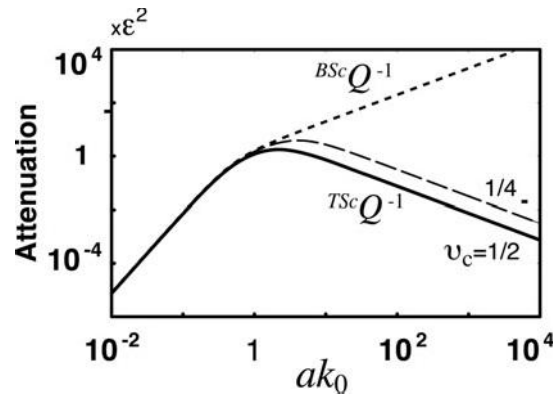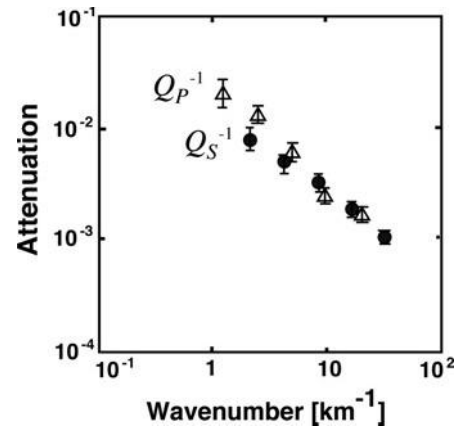(Yoshimoto et al. 1993,
copyright by Willey)

Fig. 5.5 Scattering attenuation vs. scaled wavenumber ak_0 for scalar waves in random media characterized by an exponential ACF, where $k_0 = \omega/V_0$. A dotted line is for the conventional Born approximation, a solid line ($\upsilon_c = 1/2$) and a broken line ($\upsilon_c = 1/4$) are for the travel-time corrected Born approximation

a prediction that Q_S^{-1} increases with frequency, as shown by a dotted line in Fig. 5.5. There have been two attempts to resolve the discrepancy between observations that Q_S^{-1} decreases with frequency above 0.5 Hz and the scattering theory, which predicts that Q_S^{-1} increases with frequency. One improves the statistical averaging procedure by isolating the effect of the travel-time fluctuation caused by slowly varying velocity fluctuation from other scattering phenomena that are caused by more rapidly varying velocity inhomogeneities (Sato 1982a,b); the second attempt neglects scattering in the forward direction during calculation of the attenuation (Wu 1982b). Using scalar wave propagation as an example, we will demonstrate the discrepancy between attenuation observations and the theory based on the conventional Born approximation and show how the two proposals to resolve the discrepancy are implemented. We will show that the two approaches are equivalent, and then we will extend the analysis to elastic waves.

5.3.1 Travel-Time Corrected Born Approximation for Scalar Waves

5.3.1.1 Problem of Conventional Born Approximation

Here, we study the scattering attenuation of scalar waves that travel through a randomly inhomogeneous medium. Using an ensemble of random media $\{\xi(\mathbf{x})\}$, we can statistically calculate the scattering coefficient g from the PSDF using the Born approximation. The integral over the solid angle of the average of the squared scattering amplitude over an ensemble of random media is identified as the scattering energy loss from the incident plane wave. By using (4.26), the scattered wave energy generated per unit time by a cube of inhomogeneity having volume L^3 is given by $\omega^2 V_0 \oint d\Omega\, r^2 \left(gL^3/4\pi r^2 \right) = \omega^2 V_0 g_0 L^3$, where the incident energy-flux having unit amplitude passing through an area L^2 is $\omega^2 V_0 L^2$. The fractional scattering attenuation of the incident-wave energy per unit travel distance is thus equal to g_0. Dividing g_0 by k_0, we get the scattering attenuation based on the conventional Born approximation (Aki and Richards 1980; Chernov 1960, p.742) as

$$
\begin{aligned}
{}^{BSc}Q^{-1}(\omega) &\equiv \frac{1}{k_0} g_0 = \frac{1}{4\pi k_0} \oint g\, d\Omega\, (\psi, \zeta) = \frac{1}{k_0} \oint \frac{1}{L^3} \left\langle \frac{d\sigma}{d\Omega} \right\rangle d\Omega \\
&= \frac{1}{k_0} \oint \frac{1}{L^3} \left\langle |F|^2 \right\rangle d\Omega = \frac{k_0^3}{4\pi^2} \oint P\left(2k_0 \sin\frac{\psi}{2} \right) d\Omega \\
&= \frac{k_0^3}{2\pi} \int_0^\pi P\left(2k_0 \sin\frac{\psi}{2} \right) \sin\psi\, d\psi,
\end{aligned}
\tag{5.4}
$$

where ψ is scattering angle. The prefix *"BSc"* explicitly means the attenuation due to scattering by distributed random inhomogeneities based on the conventional Born approximation. We will see the same form (7.45) for the amplitude attenuation of mean wavefield (coherent wavefield) in random media in Chap. 7.

Exponential ACF

In the case that the random media are characterized by an exponential ACF, substituting (2.11) for the PSDF, we may write the above integral as

$$
\begin{aligned}
{}^{BSc}Q^{-1}(\omega) &= 4\varepsilon^2 a^3 k_0^3 \int_0^\pi \frac{2\sin\frac{\psi}{2}\cos\frac{\psi}{2}}{\left(1 + 4a^2 k_0^2 \sin^2\frac{\psi}{2} \right)^2} d\psi = 4\varepsilon^2 a^3 k_0^3 \int_0^2 \frac{\upsilon}{\left(1 + a^2 k_0^2 \upsilon^2 \right)^2} d\upsilon \\
&= \frac{-2\varepsilon^2 a k_0}{1 + a^2 k_0^2 \upsilon^2}\bigg|_0^2 = \frac{8\varepsilon^2 a^3 k_0^3}{1 + 4a^2 k_0^2} \approx \begin{cases} 8\varepsilon^2 a^3 k_0^3 & \text{for} \quad ak_0 \ll 1 \\ 2\varepsilon^2 a k_0 & \text{for} \quad ak_0 \gg 1, \end{cases}
\end{aligned}
\tag{5.5}
$$

where $\upsilon = 2 \sin(\psi/2)$ in the first line. The scattering attenuation is proportional to the MS fractional fluctuation of velocity. The dotted line in Fig. 5.5 shows the predicted scattering attenuation against normalized wavenumber ak_0. It is proportional to the cube of wavenumber or frequency for low frequencies, and it increases linearly with frequency for high frequencies. Even if the MS fractional fluctuation is small, (5.5) predicts a larger attenuation for large ak_0 compared to that for small ak_0, which does not agree with observations like those shown in Fig. 5.1.

Theoretically predicted large scattering attenuation for high frequencies is caused by strong forward scattering. The Born approximation is valid only when the energy loss per distance L is small (Aki and Richards 1980, p.742): $^{BSc}Q^{-1}k_0L \ll 1$. Replacing L with a, we get the least restrictive condition for the applicability of the Born approximation as

$$^{BSc}Q^{-1}ak_0 \ll 1. \tag{5.6}$$

At large wavenumbers, this condition is equivalent to that the phase change is small for the propagation of the range of correlation distance, $\varepsilon ak_0 < 1$.

Thought Experiment

To better understand the effects of the slowly varying velocity inhomogeneity on the prediction of scattering attenuation, consider an ensemble of wave propagation experiments through 1-D inhomogeneous media whose wave velocities vary slowly. The experiments are done for high frequencies so we choose the dominant wavelength of an incident wavelet λ_w that is much shorter than the scale length of the velocity inhomogeneity a. Figure 5.6a is a schematic diagram showing the time traces (bold curves) u obtained from these experiments for different realizations of inhomogeneous media. We expect good resemblance in waveform between differing traces; however, first arrival travel-times are expected to vary considerably from trace to trace. The bottom trace is the average over the ensemble of the traces, which corresponds to the mean wavefield $\langle u \rangle$. It differs greatly from all measured traces because of travel-time fluctuations. The amplitude of the ensemble average trace is much smaller than that of individual traces. The wave trace next to the bottom shows the wave trace u^0 in the background homogeneous medium. Each fine broken curve in Fig. 5.6a is the difference between the measured (bold) trace and the wave trace (next to the bottom) in the background homogeneous medium, which corresponds to scattered waves $u^1 \equiv u - u^0$. The ensemble average of the square of the fine broken traces (not shown), which is used to predict scattering attenuation by the conventional Born approximation, is large. A blind application of the Born approximation thus predicts a large attenuation because of the relative travel-time shift due to the long wavelength structure. Thus, we find a link between the predicted large attenuation caused by large forward scattering for high frequencies and the travel-time fluctuation caused by the velocity inhomogeneity.
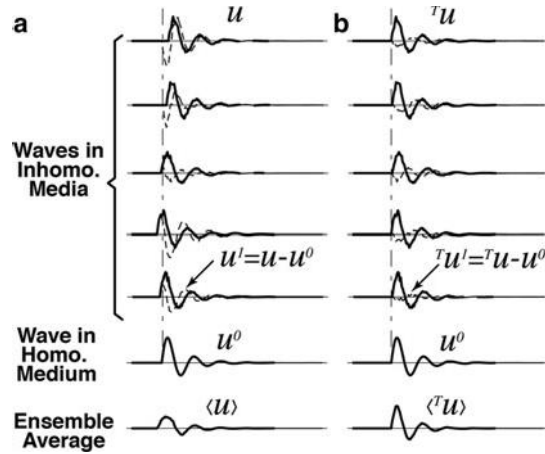
Fig. 5.6 Time traces (bold curves) u after traveling through realizations of inhomogeneous media with wavelengths longer than the dominant wavelength of the propagating wavelet λ_w. Fine broken traces show the differences u^1 from the time trace in the background homogeneous medium u^0, which is shown next to the bottom. The bottom trace is the ensemble average: (**a**) conventional Born approximation, (**b**) travel-time corrected Born approximation

Seismological attenuation measurements are done by measuring amplitudes of pulse-like direct waves irrespective of travel-times because travel-time fluctuations are unobservable on individual seismograms. Ignoring travel-time fluctuations is similar to correcting for them, so that waveforms $^T u$ appear aligned, as illustrated in Fig. 5.6b. The ensemble average trace after travel-time correction $\langle ^T u \rangle$ is shown at the bottom. The difference between each observed trace and the wave trace in the homogeneous medium $^T u^1 \equiv {}^T u - u^0$ has a small amplitude, as shown by a fine broken curve. Since the difference is small, we find that predicted scattering attenuation is small. We may say that the amplitude decay of $\langle ^T u \rangle$ corresponds to the conventional measurement of amplitude attenuation in seismology (Sato 1982a,b, 1984a,b).

The stochastic treatment of wave propagation through random media has been extensively studied by using the mean wavefield theory and the smooth perturbation method (Beaudet 1970; Frisch 1968; Howe 1971a,b; Karal and Keller 1964; Sato 1979), which will be introduced in Chap. 7. Wu (1982a) showed that the mean wavefield $\langle u \rangle$ decays exponentially due to a loss of coherency at a more rapid rate than predicted by point measurements made for a single realization of the random medium. Wu (1982a,b) pointed out that the predicted attenuation of the mean wavefield is related only to the statistical treatment of the ensemble of random media and is unrelated to seismological measurement of amplitude attenuation. The relationship between the stochastic averaging procedure and the attenuation measurement in seismology has been made clear based on these studies.

We can use the results of the above thought experiment to modify the Born scattering theory to make a prediction of scattering attenuation consistent with the manner in which seismological observations are made. The following approach

is to subtract the travel-time shift caused by the long wavelength components of velocity fluctuation and then calculate scattering amplitude based on the Born approximation. Scattering attenuation will then be given by an ensemble average of the integral over the solid angle of the square of travel-time corrected scattering amplitude.

5.3.1.2   Travel-Time Corrected Born Approximation

For an incident wave with dominant wavelength λ_w, we first decompose the fractional fluctuation of wave velocity $\xi(\mathbf{x})$ into long- and short-wavelength components by choosing a cutoff wavelength $\lambda_c = \lambda_w / \upsilon_c$:

$$\xi(\mathbf{x}) = \xi^{\mathsf{L}}(\mathbf{x}) + \xi^{\mathsf{S}}(\mathbf{x}). \tag{5.7}$$

Figure 5.7 shows the concept of decomposition, which is accomplished by using the Fourier transform:

$$\xi^{L}(\mathbf{x}) \equiv \frac{1}{(2\pi)^3} \iiint_{-\infty}^{\infty} H(\upsilon_c k_0 - m)\widetilde{\xi}(\mathbf{m})e^{i\mathbf{m}\mathbf{x}}d\mathbf{m}, \tag{5.8a}$$

$$\xi^{S}(\mathbf{x}) \equiv \frac{1}{(2\pi)^3} \iiint_{-\infty}^{\infty} H(m - \upsilon_c k_0)\widetilde{\xi}(\mathbf{m})e^{i\mathbf{m}\mathbf{x}}d\mathbf{m}, \tag{5.8b}$$

where $k_0 = 2\pi/\lambda_w$ is the wavenumber of the incident wave and $\upsilon_c k_0$ is the cutoff wavenumber for the velocity fluctuation. The corresponding PSDFs are given by

$$P^{\mathsf{L}}(m) = P(m)\,H(\upsilon_c k_0 - m) \quad \text{and} \quad P^{\mathsf{S}}(m) = P(m)\,H(m - \upsilon_c k_0). \tag{5.9}$$

Then the long-wavelength component of velocity fluctuation causes a travel-time fluctuation whose size is given by a line integral along the incident ray path. For the plane wave incidence along the third axis,

$$\delta t(\mathbf{x}) = \int_{\text{Ray}}^{x_3} \left[\frac{1}{V_0} - \frac{1}{V(\mathbf{x}')}\right]_{\text{Long Wavelength Comp.}} dx_3' \approx \frac{1}{V_0} \int_{\text{Ray}}^{x_3} \xi^{\mathsf{L}}(\mathbf{x}')\,dx_3'. \tag{5.10}$$

Fig. 5.7 Decomposition of the fractional fluctuation of wave velocity into two components in the case of cutoff-wavelength $\lambda_c = 2\lambda_w$, where λ_w is the dominant wavelength
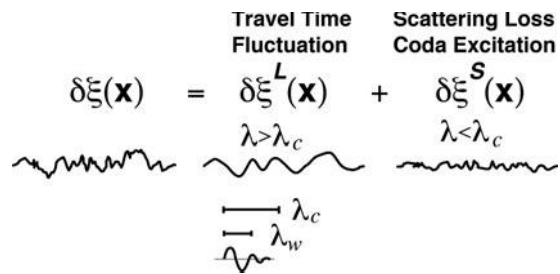
In differential form,

$$\partial_i \delta t = \frac{1}{V_0}\delta_{i3}\xi^{\mathsf{L}} \quad \text{and} \quad \partial_i \partial_j \delta t = 0, \tag{5.11}$$

where the latter condition is added to ensure that the travel-time correction term is locally constant on a plane normal to the incident ray and its second derivative with respect to the propagation direction is also zero since the spatial variation of the long-wavelength component is small (Yoshimoto et al. 1997a).

Subtracting the travel-time fluctuation δt (**x**), we can define the travel-time corrected wavefield as

$$u(\mathbf{x}, t) = {}^T u\left(\mathbf{x}, t + \delta t\ (\mathbf{x})\right), \tag{5.12}$$

where prefix "T" denotes the travel-time correction. Substituting (5.12) in (4.4) and neglecting second-order quantities, we get the wave equation

$$\left(\Delta - \frac{1}{V_0^2}\partial_t^2\right){}^T u = -\left(\frac{2}{V_0^2}\xi\partial_t^2 + 2\partial_l\delta t \cdot \partial_l\partial_t + \Delta\delta t \cdot \partial_t\right){}^T u. \tag{5.13}$$

We decompose the wavefield ${}^T u$ as

$$^T u = u^0 + {}^T u^1, \tag{5.14}$$

where $\left|{}^T u^1\right| \ll \left|u^0\right|$. Incident wave u^0 satisfies the homogeneous wave equation

$$\left(\Delta - \frac{1}{V_0^2}\partial_t^2\right)u^0 = 0. \tag{5.15}$$

Substituting unit-amplitude plane wave $u^0\ (\mathbf{x}, t) = e^{i(k_0\mathbf{e}_3\mathbf{x}-\omega t)}$ into (5.13) and using (5.11), we have

$$\left(\Delta - \frac{1}{V_0^2}\partial_t^2\right){}^T u^1 = 2k_0^2\xi^{\mathsf{S}}\ (\mathbf{x})\ e^{i(k_0\mathbf{e}_3\mathbf{x}-\omega t)}. \tag{5.16}$$

Accounting for the travel-time correction gives the result that waves are scattered only by the short-wavelength components of the inhomogeneity.

We solve the above equation under the condition that the inhomogeneity is localized in a volume having dimension L around the origin, where $L \gg a$. Using the retarded Green's function given by (4.14) and following a procedure like the one that leads to (4.18), spherically outgoing scattered wave in the far field is given by

$$^T u^1\ (\mathbf{x}, t) = \frac{e^{i(k_0 r-\omega t)}}{r}\left(\frac{-k_0^2}{2\pi}\right)\widetilde{\xi^{\mathsf{S}}}\ (k_0\mathbf{e}_r - k_0\mathbf{e}_3) = \frac{e^{i(k_0 r-\omega t)}}{r}\ {}^T F. \tag{5.17}$$

The long-wavelength component $\xi^L(\mathbf{x})$ causes travel-time fluctuation; interaction with the short-wavelength component $\xi^S(\mathbf{x})$ excites scattered waves. The travel-time corrected scattering amplitude can now be written by using the Fourier transform of the short-wavelength component of the fractional fluctuation:

$$^T F = \left(\frac{-k_0^2}{2\pi}\right) \widetilde{\xi}^S (k_0 \mathbf{e}_r - k_0 \mathbf{e}_3). \tag{5.18}$$

Substituting (5.18) into (4.25) we get the travel-time corrected scattering coefficient as

$$\begin{aligned}
^T g(\psi, \zeta; \omega) &\equiv \frac{4\pi}{L^3}\left\langle \left|^T F\right|^2\right\rangle = \frac{k_0^4}{\pi} P^S (k_0 \mathbf{e}_r - k_0 \mathbf{e}_3) \\
&= \frac{k_0^4}{\pi} P(k_0 \mathbf{e}_r - k_0 \mathbf{e}_3) H(|k_0 \mathbf{e}_r - k_0 \mathbf{e}_3| - v_c k_0) \\
&= \frac{k_0^4}{\pi} P\left(2k_0 \sin\frac{\psi}{2}\right) H(\psi - \psi_c),
\end{aligned} \tag{5.19}$$

where ψ_c is the cutoff scattering angle corresponding to the cutoff wavenumber in (5.8):

$$\psi_c \equiv 2\sin^{-1}\frac{v_c}{2}. \tag{5.20}$$

Integrating (5.19) over solid angle as (5.4), we get the scattering attenuation as

$$\begin{aligned}
^{TSc} Q^{-1}(\omega) &= \frac{1}{4\pi k_0} \oint {}^T g(\psi, \zeta; \omega)\, d\Omega(\psi, \zeta) = \frac{k_0^3}{2\pi}\int_0^\pi P^S\left(2k_0\sin\frac{\psi}{2}\right)\sin\psi\, d\psi \\
&= \frac{k_0^3}{2\pi}\int_{\psi_c}^\pi P\left(2k_0\sin\frac{\psi}{2}\right)\sin\psi\, d\psi = \frac{k_0^3}{2\pi}\int_{v_c}^2 P(k_0 v)\, v\, dv,
\end{aligned} \tag{5.21}$$

where prefix *"TSc"* denotes scattering attenuation based on the travel-time corrected Born approximation. Adjusting for the travel-time fluctuation resulted in the introduction of a lower bound for the integral that reduces the scattering attenuation for large wavenumbers, that is, the travel-time correction is equivalent to neglecting the contribution of large forward scattering within a cutoff scattering angle when calculating scattering attenuation.

Exponential ACF

When random media are characterized by an exponential ACF, we have

$$^{TSc} Q^{-1}(\omega) = 4\varepsilon^2 a^3 k_0^3 \int_{v_c}^2 \frac{v}{\left(1 + a^2 k_0^2 v^2\right)^2} dv = \frac{2\varepsilon^2 a^3 k_0^3 \left(4 - v_c^2\right)}{\left(1 + v_c^2 a^2 k_0^2\right)\left(1 + 4a^2 k_0^2\right)}$$

$$\approx \begin{cases} 2\left(4 - \upsilon_c^2\right)\varepsilon^2 a^3 k_0^3 & \text{for} \quad ak_0 \ll 1, \\ \dfrac{\left(4 - \upsilon_c^2\right)}{2\upsilon_c^2}\dfrac{\varepsilon^2}{ak_0} & \text{for} \quad ak_0 \gg 1. \end{cases} \tag{5.22}$$

The resultant scattering attenuation decreases with increasing frequency for high frequencies. We plot the travel-time corrected scattering attenuation for $\upsilon_c = 1/2$ (solid) and $1/4$ (broken) in Fig. 5.5. As υ_c decreases, the travel-time correction becomes weaker and scattering attenuation increases, particularly for larger wavenumbers. The minimum cutoff wavelength λ_c, for which a wave having wavelength λ_w will have the same sign of travel-time fluctuation over its wavelength, is $2\lambda_w$. This corresponds to $\upsilon_c = 1/2$ and $\psi_c \equiv 2\sin^{-1}\left(\upsilon_c/2\right) \approx 29°$ (Sato 1982a,b). We will use this value in the following. Then, (5.22) becomes

$$^{TSc}Q^{-1}(\omega) = \frac{15\varepsilon^2 a^3 k_0^3}{2\left(1 + \frac{1}{4}a^2 k_0^2\right)\left(1 + 4a^2 k_0^2\right)}$$

$$\approx \begin{cases} \dfrac{15}{2}\varepsilon^2 a^3 k_0^3 & \text{for} \quad ak_0 \ll 1 \\ \dfrac{15\varepsilon^2}{2ak_0} & \text{for} \quad ak_0 \gg 1, \end{cases} \tag{5.23}$$

where $^{TSc}Q_{Max}^{-1} \approx 1.8\,\varepsilon^2$ at $ak_0 \approx 2.2$. Thus, correcting for the travel-time fluctuation, we get scattering attenuation that has a peak whose amplitude is of the order of the MS fractional fluctuation and that decreases with the reciprocal of frequency for high frequencies.

For the calculation of attenuation, Chernov [1960, p.56] proposed to integrate outside of angle $\psi_c = 1/ak_0$, by arguing that forward scattering causes only phase fluctuations. Wu (1982b) proposed a method to calculate the scattering attenuation specifying $\psi_c = 90°$ in (5.21) by arguing that this is the back-scattered energy, which is lost, and that forward scattered energy is not lost. Wu's (1982b) proposal corresponds to $\upsilon_c = \sqrt{2}$, which gives a smaller peak attenuation for the same fractional velocity fluctuation. Dainty (1984) and Menke (1984a) discussed the general relationship between the spectra of inhomogeneity and corresponding scattering attenuation in the frequency domain.

Travel-Time Fluctuation

The travel-time fluctuation (5.10) does not contain diffraction effects. Taking the third axis as the incident ray direction and writing $\mathbf{x} = (\mathbf{x}_\perp, z)$, we get the MS travel-time fluctuation caused by long wavelength velocity fluctuations for travel distance $Z \gg a$ as

$$\langle\delta t(Z)^2\rangle = \frac{1}{V_0^2}\int_0^Z\int_0^Z\left\langle\xi^{\mathsf{L}}\left(\mathbf{x}'_\perp=0,z'\right)\xi^{\mathsf{L}}\left(\mathbf{x}''_\perp=0,z''\right)\right\rangle dz'dz''$$

$$= \frac{1}{V_0^2}\int_0^Z dz_d\int_{z_d/2}^{Z-z_d/2}dz_c\,R^{\mathsf{L}}\left(\mathbf{x}_\perp=0,z_d\right)$$

$$+ \frac{1}{V_0^2}\int_{-Z}^0 dz_d\int_{-z_d/2}^{Z+z_d/2}dz_c\,R^{\mathsf{L}}\left(\mathbf{x}_\perp=0,z_d\right)$$

$$= \frac{2}{V_0^2}\int_0^Z dz_d\,R^{\mathsf{L}}\left(\mathbf{x}_\perp=0,z_d\right)(Z-z_d)\approx\frac{Z}{V_0^2}\int_{-\infty}^{\infty}dz_d\,R^{\mathsf{L}}\left(\mathbf{x}_\perp=0,z_d\right)$$

$$= \frac{Z}{2\pi V_0^2}\int_0^{\infty}P^{\mathsf{L}}\left(\mathbf{m}_\perp,m_z=0\right)m_\perp dm_\perp$$

$$= \frac{Z}{2\pi V_0^2}\int_0^{\upsilon_c k_0}P\left(\mathbf{m}_\perp,m_z=0\right)m_\perp dm_\perp, \tag{5.24}$$

where $z'=z_c+z_d/2$ and $z''=z_c-z_d/2$ in the second line.

For an exponential ACF,

$$\langle\delta t(Z)^2\rangle = \frac{Z}{V_0^2}\frac{1}{2\pi}\int_0^{\upsilon_c k_0}\frac{8\pi\varepsilon^2 a^3}{\left(1+a^2 m_\perp^2\right)^2}m_\perp dm_\perp = \frac{2\varepsilon^2 aZ}{V_0^2}\frac{a^2 k_0^2\upsilon_c^2}{1+a^2 k_0^2\upsilon_c^2}$$

$$\approx\frac{2\varepsilon^2 a}{V_0^2}Z\quad\text{for}\quad ak_0\gg1. \tag{5.25}$$

For a Gaussian ACF,

$$\left\langle\delta t\left(Z\right)^2\right\rangle = \frac{Z}{V_0^2}\frac{1}{2\pi}\int_0^{\upsilon_c k_0}\varepsilon^2 a^3\sqrt{\pi^3}e^{-a^2 m_\perp^2/4}m_\perp dm_\perp$$

$$= \frac{\sqrt{\pi}\varepsilon^2 aZ}{V_0^2}\left(1-e^{-\upsilon_c a^2 k_0^2/4}\right)\approx\frac{\sqrt{\pi}\varepsilon^2 aZ}{V_0^2}\quad\text{for}\quad ak_0\gg1. \tag{5.26}$$

The MS travel-time fluctuation linearly increases with increasing travel distance. The travel-time fluctuation will be discussed in relation to the phase fluctuation in the parabolic approximation in Chap. 9.

5.3.2 Travel-Time Corrected Born Approximation for Vector Waves

Following the procedure used for scalar waves, we will now describe the procedure to correct for travel-time fluctuation due to long wavelength velocity structure to

estimate scattering attenuation for vector waves that is consistent with seismological observation methods. We define the travel-time corrected vector wavefield $^T\mathbf{u}$, which is related to vector wavefield $\mathbf{u}$ as

$$\mathbf{u}(\mathbf{x}, t) = {}^T\mathbf{u}(\mathbf{x}, t + \delta t(\mathbf{x})), \qquad (5.27)$$

where travel-time fluctuation $\delta t = \delta t^P$ or δt^S for incident plane P- or S-waves propagating to the third direction, respectively. Substituting (5.27) in (4.36), we get the wave equation for $^T\mathbf{u}$ as

$$
\begin{aligned}
\rho_0 {}^T\ddot{u}_i = & \left[\lambda_0 \partial_i \partial_j {}^T u_j + \mu_0 \partial_j \left(\partial_i {}^T u_j + \partial_j {}^T u_i \right) \right] \\
& - \delta\rho {}^T\ddot{u}_i + \partial_i \delta\lambda \partial_j {}^T u_j + \partial_j \delta\mu \left(\partial_i {}^T u_j + \partial_j {}^T u_i \right) \\
& + \delta\lambda \partial_i \partial_j {}^T u_j + \delta\mu \partial_j \left(\partial_i {}^T u_j + \partial_j {}^T u_i \right) \\
& + (\lambda_0 + \mu_0) \left(\partial_i \delta t \cdot \partial_j {}^T\ddot{u}_j + \partial_j \delta t \cdot \partial_i {}^T\ddot{u}_j \right) + 2\mu_0 \partial_j \delta t \cdot \partial_j {}^T\ddot{u}_i \\
& + (\lambda_0 + \mu_0) \partial_i \partial_j \delta t \cdot {}^T\ddot{u}_j + \mu_0 \Delta \delta t \cdot {}^T\ddot{u}_i,
\end{aligned}
\qquad (5.28)
$$

where terms of the second power of δt or higher order and cross terms of δt and fluctuations of elastic coefficients are neglected. We solve (5.28) using the first-order perturbation method. We decompose the vector wave into the incident plane wave that satisfies the homogeneous equation (4.42) and the scattered wave having small amplitude:

$$^T\mathbf{u} = \mathbf{u}^0 + {}^T\mathbf{u}^1, \qquad (5.29)$$

where $\left| {}^T\mathbf{u}^1 \right| \ll \left| \mathbf{u}^0 \right|$. The perturbation term satisfies

$$\rho_0 {}^T\ddot{u}_i^1 - \partial_j T_{ij} \left(\lambda_0, \mu_0; {}^T u_l^1 \right) = \delta f_i(\mathbf{x}, t) + {}^c\delta f_i(\mathbf{x}, t), \qquad (5.30)$$

where T_{ij} is the stress tensor, the first term on the right-hand side is the equivalent body force due to the inhomogeneity given by (4.44), and the second term is the equivalent body force corresponding to the travel-time correction:

$$
\begin{aligned}
{}^c\delta f_i(\mathbf{x}, t) = & (\lambda_0 + \mu_0) \left(\partial_i \delta t \cdot \partial_j \dot{u}_j^0 + \partial_j \delta t \cdot \partial_i \dot{u}_j^0 \right) + 2\mu_0 \partial_j \delta t \cdot \partial_j \dot{u}_i^0 \\
& + (\lambda_0 + \mu_0) \partial_i \partial_j \delta t \cdot \dot{u}_j^0 + \mu_0 \Delta \delta t \cdot \dot{u}_i^0.
\end{aligned}
\qquad (5.31)
$$

We first decompose the fluctuation of P-wave velocity into long- and short-wavelength components as

$$\delta\alpha(\mathbf{x}) = \delta\alpha^L(\mathbf{x}) + \delta\alpha^S(\mathbf{x}), \qquad (5.32)$$

where

$$\delta\alpha^{\mathsf{L}}\left(\mathbf{x}\right) \equiv \frac{1}{(2\pi)^3} \iiint_{-\infty}^{\infty} H\left(\upsilon_c k_0 - m\right) \delta\widetilde{\alpha}\left(\mathbf{m}\right) e^{i\mathbf{m}\mathbf{x}} d\mathbf{m},$$

$$\delta\alpha^{\mathsf{S}}\left(\mathbf{x}\right) \equiv \frac{1}{(2\pi)^3} \iiint_{-\infty}^{\infty} H\left(m - \upsilon_c k_0\right) \delta\widetilde{\alpha}\left(\mathbf{m}\right) e^{i\mathbf{m}\mathbf{x}} d\mathbf{m}, \tag{5.33}$$

where $\upsilon_c k_0$ is the cutoff wavenumber for a given angular frequency. For a plane P-wave propagating along the third axis, the travel-time fluctuation satisfies

$$\partial_i \delta t^P = \delta_{i3} \frac{\delta\alpha^{\mathsf{L}}}{\alpha_0^2} \quad \text{and} \quad \partial_i \partial_j \delta t^P = 0. \tag{5.34}$$

The last condition allows us to neglect the second line of (5.31). Combining (5.31) and (5.34) for an incident plane P-wave of unit amplitude propagating along the third direction (4.45), we obtain

$$^c\delta f_i^{\ P}\left(\mathbf{x}, t\right) = 2k_0\omega\rho_0\delta\alpha^{\mathsf{L}}\left(\mathbf{x}\right)\delta_{i3}e^{i(k_0\mathbf{e}_3\mathbf{x}-\omega t)}. \tag{5.35}$$

Solving (5.30) for body forces (5.35) and (4.46), we get scattered waves as outgoing spherical waves from the inhomogeneity. Then, the travel-time corrected PP-scattering amplitude having prefix "T" is given as a sum of terms given by (4.57) and correction terms:

$$^T F_{r,\psi,\zeta}^{PP} = F_{r,\psi,\zeta}^{PP} + {^c}F_{r,\psi,\zeta}^{PP}, \tag{5.36}$$

where the correction terms having prefix "c" are

$$\begin{aligned}
^c F_r^{PP} &= \frac{l_0^2}{4\pi} \frac{2}{\gamma_0^2} \cos\psi \frac{\delta\widetilde{\alpha}^{\mathsf{L}}\left(k_0\mathbf{e}_r - k_0\mathbf{e}_3\right)}{\alpha_0} \\
&= \frac{l_0^2}{4\pi} \frac{2}{\gamma_0^2} \cos\psi \; H\left(\psi_c - \psi\right) \frac{\delta\widetilde{\alpha}\left(k_0\mathbf{e}_r - k_0\mathbf{e}_3\right)}{\alpha_0} \\
^c F_\psi^{PP} &= {^c}F_\zeta^{PP} = 0.
\end{aligned} \tag{5.37}$$

In the same manner, the fluctuation of S-wave velocity is decomposed to

$$\delta\beta(\mathbf{x}) = \delta\beta^{\mathsf{L}}(\mathbf{x}) + \delta\beta^{\mathsf{S}}(\mathbf{x}), \tag{5.38}$$

where

$$\delta\beta^{\mathsf{L}}\left(\mathbf{x}\right) \equiv \frac{1}{(2\pi)^3} \iiint_{-\infty}^{\infty} H\left(\upsilon_c l_0 - m\right) \delta\widetilde{\beta}\left(\mathbf{m}\right) e^{i\mathbf{m}\mathbf{x}} d\mathbf{m},$$

$$\delta\beta^{\mathsf{S}}\left(\mathbf{x}\right) \equiv \frac{1}{(2\pi)^3} \iiint_{-\infty}^{\infty} H\left(m - \upsilon_c l_0\right) \delta\widetilde{\beta}\left(\mathbf{m}\right) e^{i\mathbf{m}\mathbf{x}} d\mathbf{m}, \tag{5.39}$$

where $\upsilon_c l_0$ is the cutoff wavenumber for a given angular frequency. For the incidence of unit amplitude plane S-wave polarized in the first direction propagating along the third axis, the travel-time fluctuation satisfies

$$\partial_i \delta t^S = \delta_{i3} \frac{\delta\beta^{\mathsf{L}}\left(\mathbf{x}\right)}{\beta_0^2} \quad \text{and} \quad \partial_i \partial_j \delta t^S = 0, \tag{5.40}$$

and the equivalent body force term is

$${}^c\delta f_i^{\ S}\left(\mathbf{x}, t\right) = 2l_0 \omega \rho_0 \delta\beta^{\mathsf{L}}\left(\mathbf{x}\right) \delta_{i1} e^{i\left(l_0 \mathbf{e}_3 \mathbf{x} - \omega t\right)}. \tag{5.41}$$

Solving (5.30) for body forces (5.41) and (4.48), we get the scattered waves as outgoing spherical waves from the inhomogeneity. The travel-time corrected SS-scattering amplitude is given as a sum of terms given by (4.57) and correction terms:

$${}^T F_{r,\psi,\zeta}^{SS} = F_{r,\psi,\zeta}^{SS} + {}^c F_{r,\psi,\zeta}^{SS}, \tag{5.42}$$

where the correction terms are

$$\begin{aligned}
{}^c F_\psi^{SS} &= \frac{l_0^2}{4\pi} 2 \cos\zeta \cos\psi \ H\left(\psi_c - \psi\right) \frac{\delta\widetilde{\beta}\left(l_0\mathbf{e}_r - l_0\mathbf{e}_3\right)}{\beta_0}, \\
{}^c F_\zeta^{SS} &= \frac{l_0^2}{4\pi} \left(-2\sin\zeta\right) H\left(\psi_c - \psi\right) \frac{\delta\widetilde{\beta}\left(l_0\mathbf{e}_r - l_0\mathbf{e}_3\right)}{\beta_0}, \\
{}^c F_r^{SS} &= 0.
\end{aligned} \tag{5.43}$$

The correction terms for both P- and S-waves are nonzero only within a cone in the forward direction satisfying $\psi < \psi_c$. Correction terms (5.37) and (5.43) are slightly different from the corresponding correction terms in Sato (1984a) because of the second condition of (5.34) and (5.40), but the following results are quantitatively similar to those given in Sato (1984a, 1990).

We have assumed that the fractional fluctuations for α and β are given by one isotropic and homogeneous random function $\xi\left(\mathbf{x}\right)$ as in (4.58). Using Birch's law, the fractional fluctuation of density is taken to be proportional to $\xi\left(\mathbf{x}\right)$ as given by (4.59). Then, combining (4.61) with (5.36), (5.37), (5.42), and (5.43), we obtain travel-time corrected scattering amplitudes by using the Fourier transform of $\xi\left(\mathbf{x}\right)$, where the argument is the exchanged wavenumber vector corresponding to each scattering mode:

$$
{}^{T}F_r^{PP} = \frac{l_0^2}{4\pi} \; {}^{T}X_r^{PP}\,(\psi, \zeta)\,\widetilde{\xi}\,(k_0\mathbf{e}_r - k_0\mathbf{e}_3)\,,
$$

$$
F_\psi^{PS} = \frac{l_0^2}{4\pi} \; X_\psi^{PS}\,(\psi, \zeta)\,\widetilde{\xi}\,(l_0\mathbf{e}_r - k_0\mathbf{e}_3)\,,
$$

$$
F_r^{SP} = \frac{l_0^2}{4\pi} \; X_r^{SP}\,(\psi, \zeta)\,\widetilde{\xi}\,(k_0\mathbf{e}_r - l_0\mathbf{e}_3)\,,
$$

$$
{}^{T}F_\psi^{SS} = \frac{l_0^2}{4\pi} \; {}^{T}X_\psi^{SS}\,(\psi, \zeta)\,\widetilde{\xi}\,(l_0\mathbf{e}_r - l_0\mathbf{e}_3)\,,
$$

$$
{}^{T}F_\zeta^{SS} = \frac{l_0^2}{4\pi} \; {}^{T}X_\zeta^{SS}\,(\psi, \zeta)\,\widetilde{\xi}\,(l_0\mathbf{e}_r - l_0\mathbf{e}_3)\,. \tag{5.44}
$$

Travel-time correction has been done only for PP- and SS-scattering since it is necessary only when the scattered wave and the incident wave are the same wave type. As shown in Fig. 4.6, basic scattering patterns X_*^{**} for conversion scattering have no lobes in the forward direction. Here, ${}^{T}X_*^{**}$ is a function of angle (ψ, ζ) representing the basic scattering pattern including the effect of travel-time correction:

$$
\begin{aligned}
{}^{T}X_r^{PP}\,(\psi, \zeta) = \frac{1}{\gamma_0^2} \Bigg[& \nu \left(-1 + \cos\psi + \frac{2}{\gamma_0^2}\sin^2\psi \right) - 2 \\
& + \frac{4}{\gamma_0^2}\sin^2\psi + 2\cos\psi \; H\,(\psi_c - \psi) \Bigg]\,,
\end{aligned}
$$

$$
{}^{T}X_\psi^{SS}\,(\psi, \zeta) = \cos\zeta \left[\nu\,(\cos\psi - \cos 2\psi) - 2\cos 2\psi + 2\cos\psi \; H\,(\psi_c - \psi) \right]\,,
$$

$$
{}^{T}X_\zeta^{SS}\,(\psi, \zeta) = \sin\zeta \left[\nu\,(\cos\psi - 1) + 2\cos\psi - 2\,H\,(\psi_c - \psi) \right]\,. \tag{5.45}
$$

Contrary to the scalar wave case, the travel-time correction for vector waves does not completely eliminate the contribution of scattering within a cone defined by cutoff scattering angle ψ_c around the forward direction. However, for angles smaller than ψ_c, the travel-time correction makes the scattering amplitude very small. In addition, ${}^{T}X_r^{PP} = {}^{T}X_\psi^{SS} = {}^{T}X_\zeta^{SS} = 0$ at $\psi = 0$. This means that the correction for the travel-time fluctuation is almost the same as neglecting scattering loss within a cone around the forward direction. Figure 5.8 shows the ψ dependence of basic scattering patterns for the travel-time corrected Born approximation, where $\gamma_0 = \sqrt{3}$, $\nu = 0.8$ and $\upsilon_c = 1/2$. The backward scattering coefficients remain unchanged since (5.37) and (5.43) show that the travel-time correction does not affect scattering for angles larger than the cutoff scattering angle ψ_c.

We imagine an ensemble of media having random fractional fluctuations described by $\xi\,(\mathbf{x})$. Then, we define scattering coefficients with travel-time correction as in (4.64):
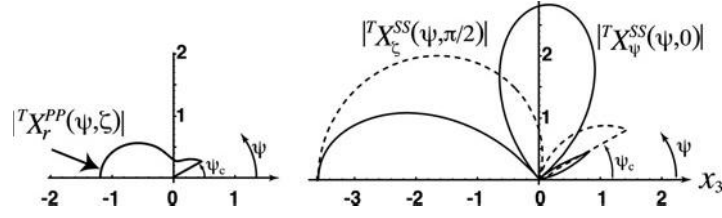
Fig. 5.8 ψ dependence of basic scattering patterns for the travel-time corrected Born approximation for $\gamma_0 = \sqrt{3}$, $\nu = 0.8$, and $\upsilon_c = 1/2$ ($\psi_c \approx 29°$). Compare with Fig. 4.6

$$
{}^{T}g^{PP}(\psi, \zeta; \omega) \equiv \frac{4\pi}{L^3} \left\langle \left| {}^{T}F_r^{PP} \right|^2 \right\rangle = \frac{l_0^4}{4\pi} \left| {}^{T}X_r^{PP} \right|^2 P\left(\frac{2l_0}{\gamma_0} \sin \frac{\psi}{2} \right),
$$

$$
{}^{T}g^{SS}(\psi, \zeta; \omega) \equiv \frac{4\pi}{L^3} \left\langle \left| {}^{T}F_\psi^{SS} \right|^2 + \left| {}^{T}F_\zeta^{SS} \right|^2 \right\rangle
$$

$$
= \frac{l_0^4}{4\pi} \left(\left| {}^{T}X_\psi^{SS} \right|^2 + \left| {}^{T}X_\zeta^{SS} \right|^2 \right) P\left(2l_0 \sin \frac{\psi}{2} \right), \tag{5.46}
$$

where the ensemble average of the squared scattering amplitude per unit volume is written by using the PSDF of the random fluctuation. Scattering loss is written as an integral of the scattering coefficient with travel-time correction over a solid angle:

$$
{}^{TSc}Q_P^{-1}(\omega) \equiv \frac{1}{4\pi k_0} \oint \left[{}^{T}g^{PP}(\psi, \zeta; \omega) + g^{PS}(\psi, \zeta; \omega) \right] d\Omega(\psi, \zeta),
$$

$$
{}^{TSc}Q_S^{-1}(\omega) \equiv \frac{1}{4\pi l_0} \oint \left[{}^{T}g^{SS}(\psi, \zeta; \omega) + g^{SP}(\psi, \zeta; \omega) \right] d\Omega(\psi, \zeta). \tag{5.47}
$$

Substituting (5.46) and (4.64) into (5.47), we finally get

$$
{}^{TSc}Q_P^{-1}(\omega) = \frac{\gamma_0 l_0^3}{(4\pi)^2} \oint \left[\left| {}^{T}X_r^{PP}(\psi, \zeta) \right|^2 P\left(\frac{2l_0}{\gamma_0} \sin \frac{\psi}{2} \right) \right.
$$

$$
\left. + \frac{1}{\gamma_0} \left| X_\psi^{PS}(\psi, \zeta) \right|^2 P\left(\frac{l_0}{\gamma_0} \sqrt{1 + \gamma_0^2 - 2\gamma_0 \cos \psi} \right) \right] d\Omega(\psi, \zeta),
$$

$$
{}^{TSc}Q_S^{-1}(\omega) = \frac{l_0^3}{(4\pi)^2} \oint \left\{ \left[\left| {}^{T}X_\psi^{SS}(\psi, \zeta) \right|^2 + \left| {}^{T}X_\zeta^{SS}(\psi, \zeta) \right|^2 \right] P\left(2l_0 \sin \frac{\psi}{2} \right) \right.
$$

$$
\left. + \gamma_0 \left| X_r^{SP}(\psi, \zeta) \right|^2 P\left(\frac{l_0}{\gamma_0} \sqrt{1 + \gamma_0^2 - 2\gamma_0 \cos \psi} \right) \right\} d\Omega(\psi, \zeta). \tag{5.48}
$$

For PS- and SP-conversion scattering, the argument of the PSDF in (5.48) cannot take a value smaller than $(\gamma_0 - 1)\, l_0/\gamma_0$, which means that only the short-wavelength components of the random inhomogeneity contribute to scattering loss.

Exponential ACF

For the case of an exponential ACF, substituting the PSDF (2.11) in (5.48), we numerical evaluate scattering attenuation as follows. The peak values are

$$
\begin{aligned}
{}^{TSc}Q^{-1}_{P\,Max} &\approx 1.6\,\varepsilon^2 \quad \text{at} \quad a\omega/\beta_0 \approx 3.0, \\
{}^{TSc}Q^{-1}_{S\,Max} &\approx 1.0\,\varepsilon^2 \quad \text{at} \quad a\omega/\beta_0 \approx 2.0.
\end{aligned}
\tag{5.49}
$$

For low frequencies, $a\omega/\beta_0 \ll 1$,

$$
{}^{TSc}Q^{-1}_P \approx 4.7\,\varepsilon^2 \left(\frac{a\omega}{\beta_0}\right)^3 \quad \text{and} \quad {}^{TSc}Q^{-1}_S \approx 7.2\,\varepsilon^2 \left(\frac{a\omega}{\beta_0}\right)^3,
\tag{5.50}
$$

where ${}^{TSc}Q^{-1}_P/{}^{TSc}Q^{-1}_S \approx 0.66$. For high frequencies, $a\omega/\beta_0 \gg 1$,

$$
{}^{TSc}Q^{-1}_P \approx 10\,\varepsilon^2 \left(\frac{\beta_0}{a\omega}\right) \quad \text{and} \quad {}^{TSc}Q^{-1}_S \approx 4.6\,\varepsilon^2 \left(\frac{\beta_0}{a\omega}\right),
\tag{5.51}
$$

where ${}^{TSc}Q^{-1}_P/{}^{TSc}Q^{-1}_S \approx 2.2$. Thus, scattering attenuation decreases according to the reciprocal of frequency for both P- and S-waves.

Figure 5.9 shows the frequency dependence of scattering attenuation for P-waves, S-waves, and their ratio, where the abscissa is scaled S-wave wavenumber $al_0 = a\omega/\beta_0$. Ratio ${}^{TSc}Q^{-1}_P/{}^{TSc}Q^{-1}_S$ is smaller than 1 for lower frequencies; however, it becomes larger than 1 for higher frequencies. Comparing contributions of different scattering modes, we find that SS scattering is dominant in S-wave attenuation (see Sato 1984a, Fig. 10).

We plot the theoretical S-to-S backscattering coefficient g^{SS}_π (4.68) for an exponential ACF with $\varepsilon^2 = 0.01$ and $a = 2\,\text{km}$ by a solid curve along with both backscattering coefficient and total scattering coefficient measured from S-coda excitation of local earthquakes from various regions of the world in Fig. 5.10. We plot the theoretical scattering attenuation of S-waves ${}^{TSc}Q^{-1}_S$ and ratio ${}^{TSc}Q^{-1}_P/{}^{TSc}Q^{-1}_S$ by solid curves along with worldwide observations in Fig. 5.11. The theoretical curves provide a good fit to the observed data. The PSDF of velocity fractional fluctuation corresponding to this estimate is plotted by line 5.1 in Fig. 1.4.
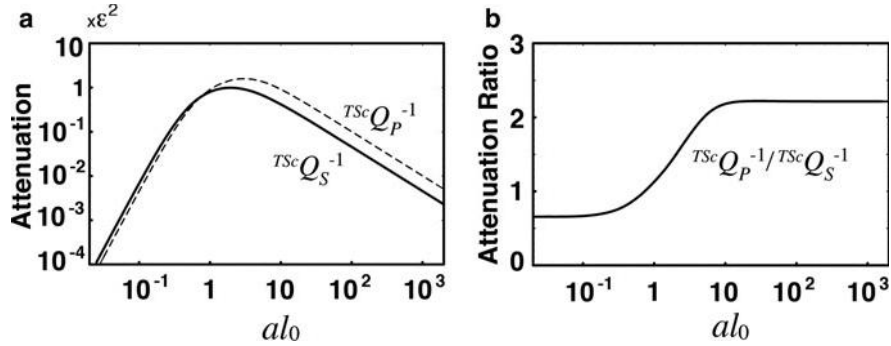
Fig. 5.9 (a) Frequency dependence of scattering attenuation $^{TSc}Q_S^{-1}$ (solid curve) and $^{TSc}Q_P^{-1}$ (broken curve) and (b) ratio of $^{TSc}Q_P^{-1}$ to $^{TSc}Q_S^{-1}$ theoretically predicted by the travel-time corrected Born approximation for an exponential ACF ($\kappa = 0.5$) for $\gamma_0 = \sqrt{3}$, $\nu = 0.8$, and $\upsilon_c = 1/2$ ($\psi_c \approx 29°$), where $l_0 = \omega/\beta_0$

Fig. 5.10 S-to-S backscattering coefficient g_π^{SS} vs. frequency, where $\beta_0 = 4$km/s, $\gamma_0 = \sqrt{3}$, $\nu = 0.8$: a solid curve for the exponential ACF ($\kappa = 0.5$, $\varepsilon^2 = 0.01$ and $a = 2$ km) and a broken curve for the von Kármán ACF ($\kappa = 0.35$, $\varepsilon^2 = 0.0072$ and $a = 2.1$ km). Background shows regional measurements of g_0 and g_π worldwide (see Fig. 1.3)
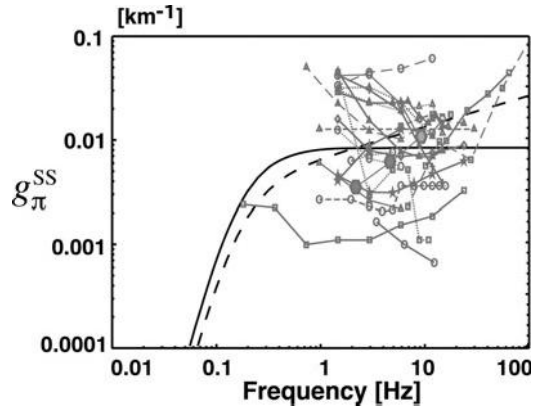
von Kármán ACF

The predicted rate of decrease in Q_S^{-1} with increasing frequency at high frequency given by (5.51) appears to be faster than observations (see Fig. 5.11a). Using data collected in the Kanto area, Japan, Sato (1984b, 1990) and Kinoshita (1994) estimated that $Q_S^{-1} \propto f^{-0.7}$. For the case of a von Kármán ACF of order κ, the scattering attenuation and the back scattering coefficient are

$$^{TSc}Q_P^{-1}, \quad ^{TSc}Q_S^{-1} \propto \varepsilon^2 \left(\frac{\beta_0}{a\omega} \right)^{2\kappa},$$

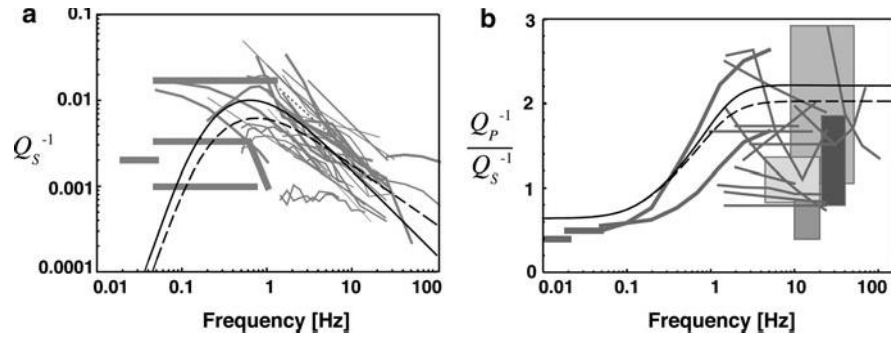$$g_\pi^{SS} \propto \frac{\varepsilon^2}{a} \left(\frac{a\omega}{\beta_0} \right)^{1-2\kappa} \tag{5.52}$$

Fig. 5.11 Plots of (**a**) $^{TSc}Q_S^{-1}$ vs. frequency and (**b**) ratio of $^{TSc}Q_P^{-1}$ to $^{TSc}Q_S^{-1}$ vs. frequency predicted by the travel-time corrected Born approximation, where $\beta_0 = 4$ km/s, $\gamma_0 = \sqrt{3}$, $\nu = 0.8$, and $\upsilon_c = 1/2$: solid curves for the exponential ACF ($\kappa = 0.5$, $\varepsilon^2 = 0.01$ and $a = 2$ km) and broken curves for the von Kármán ACF ($\kappa = 0.35$, $\varepsilon^2 = 0.0072$ and $a = 2.1$ km). Background shows regional measurements worldwide (see Figs. 5.1 and 5.3)
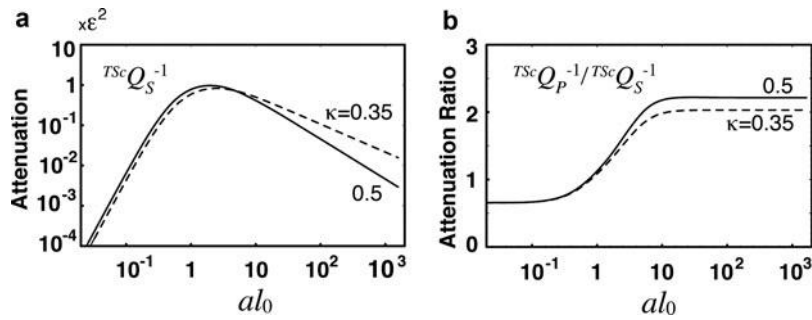

Fig. 5.12 (**a**) Frequency-dependence of predicted scattering attenuation for S-wave $^{TSc}Q_S^{-1}$ and (**b**) ratio $^{TSc}Q_P^{-1}/^{TSc}Q_S^{-1}$ for the von Kármán ACF ($\kappa = 0.35$, broken curve) and the exponential ACF ($\kappa = 0.5$, solid curve) for $\gamma_0 = \sqrt{3}$, $\nu = 0.8$, and $\upsilon_c = 1/2$ ($\psi_c \approx 29°$), where $l_0 = \omega/\beta_0$

at high frequencies $a\omega/\beta_0 \gg 1$. Figure 5.12 shows the frequency dependence of S-wave attenuation and the ratio of P- to S-wave attenuation for $\kappa = 0.35$ and $\kappa = 0.5$ (exponential ACF). For $\kappa = 0.35$ the ratio of P- to S-wave attenuation is 2.03 at high frequencies. The ratio slightly decreases as the κ-value becomes smaller. In Figs. 5.10 and 5.11, broken curves show the best fit theoretical predictions for the von Kármán ACF with $\kappa = 0.35$, $\varepsilon^2 = 0.0072$ and $a = 2.1$ km. The theoretical curves provide a good fit to the observed data. The PSDF of velocity fractional fluctuation corresponding to this estimate is plotted by line 5.2 in Fig. 1.4.

We should note that the above estimation of randomness is the maximum value since all the attenuation is supposed to be caused only by scattering due to distributed random inhomogeneities but intrinsic absorption is completely neglected.

5.3.3   Evaluation of Cutoff Scattering Angle

As shown in Fig. 5.5, the choice of cutoff scattering angle impacts the attenuation predictions made by the single scattering theory; however, the choice of cutoff angle is not self evident. Several investigators have evaluated scattering attenuation using 2-D acoustic finite difference simulations for media having random velocity fluctuation to estimate the cutoff scattering angle, or the lower bound for the integral over scattering angle. For the 2-D scalar wave case, the travel-time corrected scattering attenuation for an exponential ACF is

$$^{TSc}Q^{-1}\left(\omega\right) = \frac{k_0^2}{\pi}\int_{\psi_c}^{\pi} P\left(2k_0\sin\frac{\psi}{2}\right)d\psi = \int_{\psi_c}^{\pi}\frac{2\varepsilon^2 a^2 k_0^2}{\left(1 + 4a^2 k_0^2 \sin^2\frac{\psi}{2}\right)^{3/2}}d\psi,$$

(5.53)

where the lower bound of the angular integral ψ_c is the cutoff angle.

Frankel and Clayton (1986) measured the apparent attenuation of direct amplitude with travel distance from their 2-D numerical simulations and plotted apparent attenuation against the product of wavenumber and correlation distance for the exponential ACF with $\varepsilon = 10\%$. They found that apparent attenuation measured from their simulations roughly follows the theoretical curve given for $0.2 < ak_0 < 6$ by (5.53) when $\psi_c = 30° - 45°$. The cutoff angle ψ_c for the calculation of scattering loss was examined using numerical experiments for a wider range of medium parameters by Roth and Korn (1993). Changing ε from 3% to 9% and using an exponential ACF, they measured scattering loss from the amplitude change of an isolated pulse over travel distance in 2-D acoustic random media. Their results are shown in Fig. 5.13. For $0.2 < ak_0 < 20$, they concluded that ψ_c ranges from 20° to 40°. Studies of Frankel and Clayton (1986) and Roth and Korn (1993) provide evidence supporting the value of 29° proposed for the 3-D case. Fang and Müller

Fig. 5.13 Plot of scattering attenuation in 2-D acoustic random media vs. scaled wavenumber ak. An irregular line shows measurements made from 2-D finite difference simulations. Regular lines show predictions of (5.53) for various values of ψ_c, where $k = \omega/V_0$. Random medium is characterized by an exponential ACF with $\varepsilon = 9\%$. (Roth and Korn 1993, copyright by Willey)
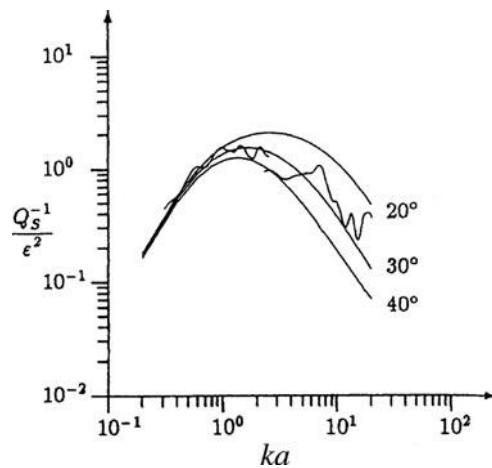
(1996) preferred that ψ_c about $20°$ for scattering attenuation based on measurements of the decay of the envelope maximum and spectral amplitude with travel distance. Kawahara (2002) investigated the constraint by causality on the choice of the cutoff angle ψ_c for scalar waves in 3-D random media. On the basis of the Kramers-Krönig relation, he derived a simple relation among ψ_c and the phase velocities in the high- and low-frequency limits c_∞ and c_0: $c_\infty/c_0 = 1 + (\varepsilon^2/2)(\mathrm{cosec}(\psi_c/2) - 1)$ irrespective of ACF type. It means $\psi_c \approx 60°$ if $c_\infty = V_0(1-\varepsilon^2)$; however, $\psi_c \approx 29°$ if $c_\infty = V_0$.

For the calculation of scattering attenuation through distributed cracks, the idea of neglecting scattering energy within a cone around the forward direction is useful. From the measurement of amplitude attenuation through an aluminum block containing parallel cylindrical voids, Dubendorff and Menke (1986) found that the apparent attenuation was well fit by the corrected scattering attenuation model when the cutoff scattering angle is $10°$ for P-waves, $6°$ for SH-waves, and $15°$ for SV-waves.

5.3.4   Diffraction Effects

The derivation of scattering attenuation by using the Born approximation can be viewed as a kind of differential approach since the correction for travel-time fluctuation is given in differential form in (5.11). Diffraction effects caused by long-wavelength components of the inhomogeneity were neglected. These diffraction effects become increasingly important as travel distance increases.

Shapiro and Kneib (1993) investigated this phenomena in detail for isotropic random acoustic media. They measured the decay of the logarithm of mean-wave (coherent-wave) amplitude $\ln\langle u \rangle$ and that of the mean logarithm of amplitude $\langle \ln A_0 \rangle$ with travel distance in a frequency range dominated by forward scattering. Regressions of $\langle \ln A_0 \rangle$ vs. travel distance are common methods for measuring attenuation in the earth. Figure 5.14a shows $\langle \ln A_0 \rangle$ and $\ln\langle u \rangle$ predicted by the parabolic approximation (see Chap. 9) at $100\,\mathrm{Hz}$ against travel distance for short travel distances in 3-D, where $100\,\mathrm{Hz}$ corresponds to a wavelength of $30\,\mathrm{m}$ and $ak_0 \approx 4.2$. $\ln\langle u \rangle$ decreases linearly with travel distance. However, $\langle \ln A_0 \rangle$ decreases more slowly and is similar to the curve predicted by Wu's (1982b) approximation for short travel distances that uses $\psi_c = 90°$ and counts scattering only into the back half-space for the estimation of scattering attenuation. This means that attenuation of the coherent wavefield is caused mainly by travel-time fluctuations but that backscattering alone is insufficient to explain the observed amplitude attenuation. Shapiro and Kneib (1993) also measured $\langle \ln A_0 \rangle$ from 2-D finite difference calculations for the scalar wave equation by taking many point measurements of the wavefield, computing the spectra, and averaging the natural logarithms. Figure 5.14b plots $\langle \ln A_0 \rangle$ vs. distance at long travel distances measured from the numerical simulations. Numerical results, represented by dots, agree well with the bold convex curve, which is predicted to be due to de-focusing of the
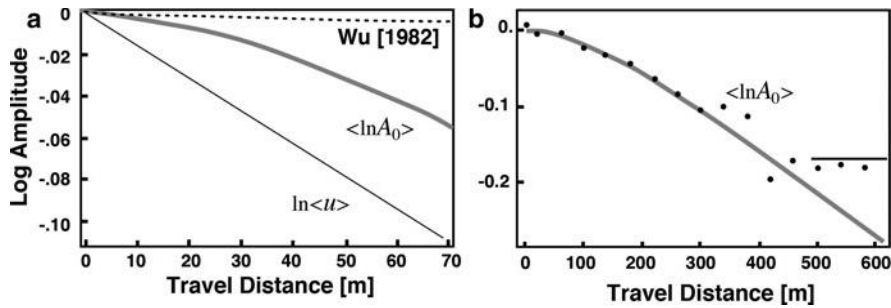
Fig. 5.14 (**a**) Plots of logarithm of mean-wave amplitude $\ln \langle u \rangle$ (solid curve) vs. travel distance of 100 Hz waves in a 3-D acoustic random medium of average velocity $V_0 = 3$ km/s having an exponential ACF with $a = 20$ m and $\varepsilon = 3\%$. A bold convex curve is $\langle \ln A_0 \rangle$ predicted from the parabolic approximation theory. A broken curve is the prediction by Wu (1982b) who used single scattering theory with $\psi_c = 90°$. (**b**) Plots of logarithm amplitude vs. travel distance of 100 Hz waves in a 2-D acoustic random medium of the same statistical characteristics as in (**a**). Dots are $\langle \ln A_0 \rangle$ measured from numerical simulations. A bold convex curve is $\langle \ln A_0 \rangle$ predicted from the parabolic approximation theory, and the horizontal bar corresponds to saturation due to strong scattering. (Shapiro and Kneib 1993, copyright by Willey)

wavefield by the parabolic approximation for the specific model structure with $a k_0 \gg 1$, where backscattering is neglected. Even though the medium fluctuation is small, at distances larger than 500 m in the simulation, the mean logarithm amplitude stays at the same level irrespective of travel distance because of the dominance of incoherent wavefield due to diffraction and forward scattering. There is a difference between the global estimate and the local estimate of attenuation. Shapiro and Kneib (1993) raised concern about the careless use of the linear regression for a long distance range to estimate the characteristics of random media.

In Chap. 9, we will statistically study the attenuation of the maximum amplitude and the broadening of envelope for the propagation of an impulsive wavelet through random media based on the parabolic wave equation.

5.4 Scattering Attenuation Due to Distributed Cracks and Cavities

As introduced in Chap. 2 microscopic cracks are known to be pervasive in crustal rocks. Several models for predicting the influence of cracks and inclusions in rocks on elastic properties have been developed since the pioneering work of Walsh (1965). Since then several models have been developed to predict the effects of empty and fluid-filled cracks on intrinsic attenuation as introduced at the beginning of this Chapter. These models were developed to predict the bulk properties of rocks, so little attention was paid to the character of the scattered wavefield. It is natural to imagine a single crack or a distribution of cracks as the heterogeneity and to investigate the characteristics of the scattered wavefield.

The finite difference method is the most common for the simulation of wavefields in an inhomogeneous medium (e.g. Alford et al. 1974; Aminzadeh et al. 1994). This approach is based on a discretization of the medium and the equations of motion describing wave propagation. Although this method is reliable for modeling wave propagation in media having relatively modest spatial variations in elastic properties, it does not work well in media that are strongly heterogeneous since derivatives are calculated as averages over many grid points in the medium, which is equivalent to assuming that the medium varies smoothly rather than having discontinuous variations in medium properties.

There have been several attempts to solve the boundary value problem for the scattered wavefield caused by plane waves incident on an isolated spherical inclusion (e.g. Einspruch et al. 1960; Korneev and Johnson 1993a,b; Yamakawa 1962; Ying and Truell 1956). Gritto et al. (1995) and Korneev and Johnson (1996) examined conversion scattering characteristics for the incidence of both P- and S-waves on a spherical inclusion. They pointed out the significant amount of P-to-S scattering compared with S-to-P scattering.

Kikuchi (1981) analytically calculated elastic wave attenuation due to distributed cracks of half-length a_c in a 2-D medium. A crack is geometrically described as the limit of an ellipse on which the stress is free. The resultant scattering attenuation Q_P^{-1} for P-waves arriving normal to the crack plane has a peak at $a_c k_0 \approx 0.64$, and the peak value is a few times larger than the peak value of scattering attenuation Q_S^{-1} for S waves. Kawahara and Yamashita (1992) used an integral equation to examine attenuation for waves at oblique incidence on a fracture zone containing randomly distributed cracks whose planes are aligned parallel to the fracture plane. Figure 5.15 shows scattering attenuation for SH-waves, where the peak frequency is almost independent of the incidence angle (Kawahara and Yamashita 1992). The higher frequency asymptote of scattering attenuation is proportional to the reciprocal of frequency. Yamashita (1990) used an integral equation to calculate SH-wave scattering attenuation through a medium composed of a distribution of cracks whose half-lengths a_c obey an inverse power of dimension and whose orientations are random. He discussed the change in scattering attenuation in relation to the
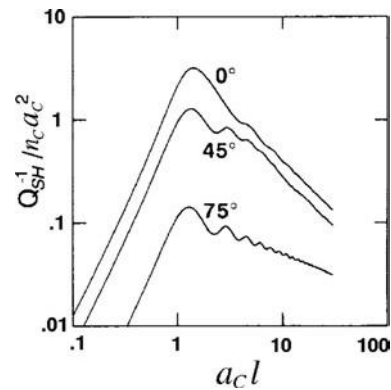
Fig. 5.15 Scattering loss due to aligned non-opening cracks with half-length a_c for SH-waves having various incident angles relative to the plane of the aligned cracks, where n_c is the number density of cracks, and $l = \omega/\beta_0$. (Kawahara and Yamashita 1992, copyright by Springer)

power of the crack size distribution. Later, using the boundary integral method, Murai et al. (1995) numerically simulated SH-wave propagation through a medium containing 72 distributed parallel plane cracks containing Newtonian viscous fluid. Matsunami (1990) measured attenuation and amplitude fluctuation of acoustic waves propagating through an aluminum plate with many clusters of small open holes. He found a peak in Q^{-1} when the wavelength is about 1.5 times the average diameter of the cluster of holes.

For all models investigated, the crack model predicts a peak in Q^{-1} when the wavelength is of the same order as the dimension of the crack. If we fit the scattering attenuation to the predicted peak in observed attenuation at 0.5 Hz as suggested in observed Q_S^{-1}, the dimension of crack a_c has to be of the order of kilometers.

Scattering attenuation due to distributed cylindrical cavities was analytically studied by using a scattering matrix by Varadan et al. (1978). Numerical synthesis of time domain seismograms for waves incident on a distribution of many open cavities was done by Benites et al. (1992). They used the boundary integral method to deterministically model multiple scattering of SH-waves in 2-D media containing a distribution of randomly spaced cylindrical cavities of radius a_c, as schematically illustrated in Fig. 5.16.

Since an exact numerical method was employed, they were able to investigate wave scattering in media containing strong velocity contrasts. The boundary integral approach used by Benites et al. (1992) was a frequency-domain implementation. The total SH-wavefield $\hat{u}(\mathbf{x}, \omega)$ at angular frequency ω obeys the Helmholtz equation:

$$\left(\Delta + l_0^2\right) \hat{u}(\mathbf{x}, \omega) = 0, \tag{5.54}$$

where wavenumber $l_0 = \omega/\beta_0$. The Green's function for a delta function source at the origin in a 2-D homogeneous medium satisfying the radiation condition is written by using the Hankel function of the first kind of the zeroth order as

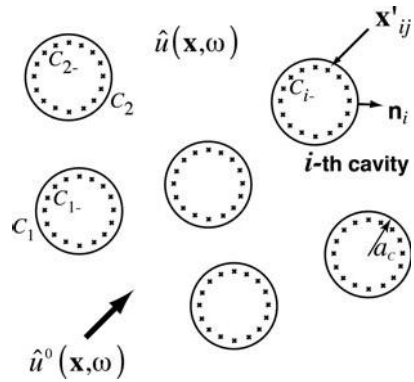$$\widehat{G}_0(\mathbf{x}, \omega) = -\frac{i}{4} H_0^{(1)}(l_0 r). \tag{5.55}$$

Fig. 5.16 Schematic illustration of distributed cylindrical cavities and the incident SH-wave $\hat{u}^0(\mathbf{x}, \omega)$, where total wavefield is given by $\hat{u}(\mathbf{x}, \omega)$

The solution of (5.54) is written in the form of an indirect integral representation, where the total wavefield is the sum of the incident wave and scattered waves from sources located along the boundaries of the M cavities:

$$\hat{u}\left(\mathbf{x}, \omega\right) = \hat{u}^0\left(\mathbf{x}, \omega\right) + \sum_{i=1}^{M} \oint_{C_{i-}} \widehat{G}_0\left(\mathbf{x} - \mathbf{x}', \omega\right) \Lambda_i\left(\mathbf{x}', \omega\right) dc_i\left(\mathbf{x}'\right), \qquad (5.56)$$

where $\mathbf{x}'$ is the location of a source Λ_i for the scattered wavefield, dc_i is an infinitesimal line element, and circle C_{i-} is interior to boundary C_i of the i-th cavity. Practically they took the radius of C_{i-} as 80% of the radius of C_i to avoid the singularity of the Green's function at the location, where boundary conditions must be met.

It is necessary to describe the boundary condition to solve (5.56) since it is a class of indirect integral representation problems. Benites et al. (1992) discretized the source distribution for the i–th cavity as

$$\Lambda_i\left(\mathbf{x}, \omega\right) = \sum_{j=1}^{N} A_{ij}\left(\omega\right) \delta\left(\mathbf{x} - \mathbf{x}'_{ij}\right), \qquad (5.57)$$

where A_{ij} is a complex constant that represents the strength of the source located at the j-th point along a circle C_{i-} of the i-th cavity $\mathbf{x}'_{ij}$ and N is the number of sources. The minimum number of sources required is $2\pi a_c/(\lambda_w/4)$ for wavelength λ_w. Then, they wrote (5.56) as

$$\hat{u}\left(\mathbf{x}, \omega\right) = \hat{u}^0\left(\mathbf{x}, \omega\right) + \sum_{i=1}^{M} \sum_{j=1}^{N} A_{ij}\left(\omega\right) \widehat{G}_0\left(\mathbf{x} - \mathbf{x}'_{ij}, \omega\right). \qquad (5.58)$$

They imposed the Neumann boundary conditions on the cavity surfaces in a least square sense. They minimized the square sum of traction along all boundaries:

$$\sum_{k=1}^{M} \oint_{C_k} \left| \mu \frac{\partial \hat{u}}{\partial \mathbf{n}_k} \right|^2 dc_k \Rightarrow \text{Min. ,} \qquad (5.59)$$

where $\mathbf{n}_k$ is the outward normal vector to boundary C_k. Substituting (5.58) in (5.59), they got a system of simultaneous linear equations for A_{ij}:

$$\sum_{i=1}^{M} \sum_{j=1}^{N} \left(\sum_{k=1}^{M} \oint_{C_k} \frac{\partial \widehat{G}^*_{0mn}}{\partial \mathbf{n}_k} \frac{\partial \widehat{G}_{0ij}}{\partial \mathbf{n}_k} dc_k \right) A_{ij} = - \sum_{k=1}^{M} \oint_{C_k} \frac{\partial \widehat{G}^*_{0mn}}{\partial \mathbf{n}_k} \frac{\partial \hat{u}^0}{\partial \mathbf{n}_k} dc_k, \qquad (5.60)$$

where an asterisk stands for complex conjugate and $\widehat{G}_{0mn}$ means $\widehat{G}_0\left(\mathbf{x} - \mathbf{x}_{mn}', \omega\right)$. The right-hand side represents the interaction between the incident wave and the
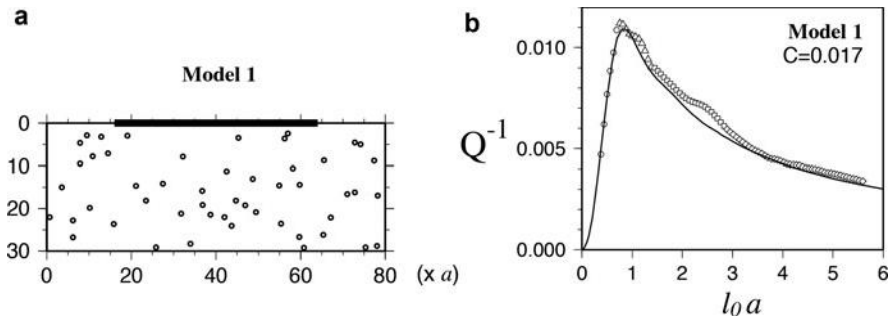
Fig. 5.17 (**a**) Configuration of 50 cavities of radius a used in numerical simulations, where SH-waves are vertically incident from below. (**b**) Scattering loss of direct SH-wave against scaled wavenumber al_0, where $l_0 = \omega / V_0$. Open symbols denote numerical experimental values. A solid line is according to the Foldy theory. (Kawahara et al. 2009, copyright by the Acoustical Society of America)

n-th source of the m-th cavity. The left-hand side represents the interaction between the n-th source of the m-th cavity and the j-th source of the i-th cavity. Solving these simultaneous linear equations in the angular-frequency domain, they got the strength of the sources A_{ij}. By using the inverse Fourier transform of the solutions obtained for many frequencies, they obtained synthetic seismograms in the time domain.

Solving the problem for the incidence of a plane wave or a line source, Benites et al. (1992) numerically synthesized seismograms for the medium containing 50 cavities. They measured the amplitude attenuation of direct SH-wave against travel distance through an infinite medium that includes a region containing distributed cavities. Their scattering attenuation measurements are well explained by the theoretical prediction that is obtained by using the optical theorem. Later Kawahara et al. (2009) numerically simulated SH waves in distributed cavities for the vertical incidence as shown in Fig. 5.17a. Scattering attenuation of peak amplitude is compared with the Foldy theory (Foldy 1945) in Fig. 5.17b. Both agree well each other in the case of small cavity density.

5.5   Further Reading

Barton [2007, Chap. 10] reviews recent measurements of seismic wave attenuation at many different scales and possible attenuation mechanisms. In Chap. 8, we will see quantitative measurements of both intrinsic and scattering attenuation from the balance of coda excitation and the direct wave amplitude attenuation on the basis of the multiple isotropic scattering model. In Chap. 9, we will see a power-law decay of the maximum amplitude of a wavelet with distance in random media according to the stochastic treatment of the parabolic-type equation when the wavelength is shorter than the correlation distance.